IEEE Photonics Journal
An IEEE Photonics Society Publication

Open Access

Nanoscale Strain Mapping in SIMOX 3-D Sculpted Silicon Waveguides Using Tip-Enhanced Raman Spectroscopy

Volume 8, Number 5, October 2016

Huashun Wen
Yuefeng Ji
Bahram Jalali, *Fellow, IEEE*

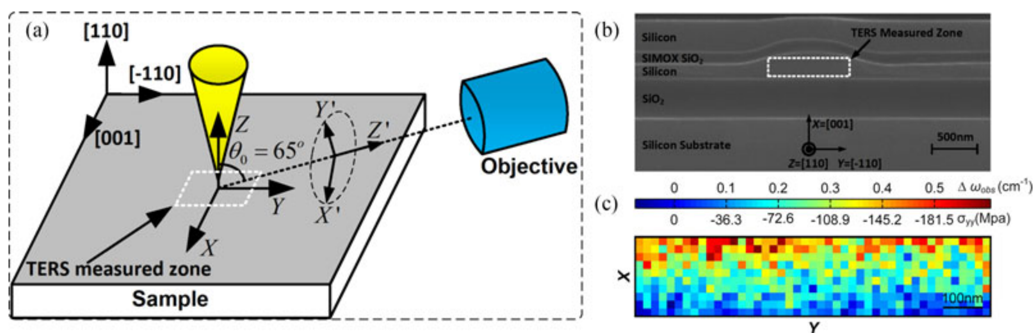

DOI: 10.1109/JPHOT.2016.2612360
1943-0655 © 2016 IEEE

IEEE photonics SOCIETY
IEEE

Nanoscale Strain Mapping in SIMOX 3-D Sculpted Silicon Waveguides Using Tip-Enhanced Raman Spectroscopy

Huashun Wen,[1] Yuefeng Ji,[1] and Bahram Jalali,[2] *Fellow, IEEE*

[1]State Key Laboratory of Information Photonics and Optical Communications, School of Information and Communication Engineering, Beijing University of Posts and Telecommunications, Beijing 100876, China
[2]Department of Electrical Engineering, University of California, Los Angeles, CA 90095 USA

DOI:10.1109/JPHOT.2016.2612360
1943-0655 © 2016 IEEE. Translations and content mining are permitted for academic research only. Personal use is also permitted, but republication/redistribution requires IEEE permission. See http://www.ieee.org/publications_standards/publications/rights/index.html for more information.

Manuscript received September 6, 2016; accepted September 19, 2016. Date of publication September 22, 2016; date of current version October 10, 2016. This work was supported by the Natural Science Foundation of China under Grant 61372118. Corresponding authors: Y. Ji and B. Jalali (e-mail: jyf@bupt.edu.cn; jalali@ucla.edu).

Abstract: Strain in silicon plays a significant role in exploring electro-optical material, boosting transistor performance, tuning birefringence of optical silicon waveguides, and so on. In this paper, we measured, for the first time, the nanoscale strain in the SIMOX 3-D sculpted silicon waveguides using tip-enhanced Raman spectroscopy (TERS). A model, which relates the observed Raman peak shifts to the localized stresses for our TERS experiments, was presented. The tip-induced electric-field enhancements, tip-induced depolarization of incident light, and oblique incidence geometry of the TERS system were included in the model. Both polarizations of incident light and Raman scattered light are selected appropriately with the guidance of the model for obtaining enough electric-field enhancements and accurately calculate the stresses. A 2-D stress map inside the silicon waveguide with spatial resolution of about 20 nm was obtained, and corresponding strains were calculated based on Hooke's law. We observed that the stresses are compressive, and the strains show inhomogeneity. The origins of strain and the strain-induced second-order optical susceptibility inside the SIMOX 3-D sculpted buried silicon waveguides are discussed and analyzed. The mapping of 2-D nanoscale strain and the analysis of second-order optical susceptibility in this work suggest that the SIMOX 3-D sculpted strained silicon might be a potential metamaterial for electro-optical modulation and optical signal processing. Moreover, the presented TERS model could be a valuable tool for probing strain in strained silicon devices.

Index Terms: Electro-optical materials, engineered photonic nanostructures, optical and other properties, Raman spectroscopy, SIMOX 3-D sculpting, strained silicon, tip-enhanced Raman spectroscopy (TERS).

1. Introduction

To accommodate the ever-increasing amount of data traffic from high-definition video, file sharing, cloud computing, and other Internet services, the future optical network will still require higher bandwidth and more energy-efficient data communication [1], [2]. Particularly, ubiquitous optical signal processing techniques, such as advanced modulation formats, signal regeneration, physical impairment mitigation techniques are needed for the physical layer of optical network [3], [4]. Silicon photonics is one of the thriving discipline, and it has tremendous potential to build and

monolithically integrate electronic and optical devices with a small footprint, low power consumption, and scalability to meet these demands of the future optical network [5]. The silicon-on-insulator (SOI) material system has proven to be an excellent platform in silicon photonics. A variety of optical functionalities including laser, modulation, amplification, signal regeneration and switching have been realized on the SOI wafers using the nonlinear processes, such as stimulated Raman scattering, plasma dispersion effect, four-wave mixing and cross phase modulation, in silicon [6]–[10]. Unfortunately, the second order optical susceptibility $\chi^{(2)}$, which is the active ingredient to realize electro-optic modulator, wavelength converter, and other optical signal processing techniques, is absent in silicon owning to the centrosymmetry of silicon crystal. However, by depositing a straining layer of silicon nitride on top of silicon, the inhomogeneous strain breaks the centrosymmetry of silicon's crystal lattice, and induces the second order optical susceptibility $\chi^{(2)}$ in silicon [11].

The $\chi^{(2)}$ in strained silicon has been measured via Pockels electro-optical modulation, and the reported $\chi^{(2)}$ values are on the order of magnitude of 100 pm/V [12]–[14]. However, these experimental $\chi^{(2)}$ values maybe wrongly interpreted and mainly as a result of the free carrier in the strained silicon [15]–[17], but not the strain. In order to avoid the effect of free carrier, high speed measurements, namely the second harmonic generation (SHG) measurements, were utilized to measure the $\chi^{(2)}$ in the strained silicon, and the values are on the order of magnitude of 10 pm/V [18]. Nevertheless, the positive fixed charges close to the Si/SiN interface causes a strong electrical-field-induced-second-harmonic (EFISH), which leads to enhancement of the SHG-measured $\chi^{(2)}$ values [19]. In addition, someone believes that the origin of the measured $\chi^{(2)}$ in the strained silicon is from the silicon nitride cladding layer but not from silicon itself [20]. On the other hand, numerous theoretical model, which describes the relation between $\chi^{(2)}$ and strain gradients inside silicon, were developed based on sp3 bond-orbital theory, symmetry arguments, and so on [15], [21], [22]. However, the theoretically calculated $\chi^{(2)}$ values are much smaller than the experimentally measured ones [23]. In order to explore the $\chi^{(2)}$ in strained silicon and support the development of the strain-induced $\chi^{(2)}$ theoretical model, the strain at the nanometer scale in the silicon waveguide should be determined. Moreover, strain in silicon has other great applications, such as boosting transistors performance [24], tuning birefringence of optical silicon waveguides [25], and so on.

Separation by IMplantation of OXygen (SIMOX) 3-D sculpting, which is a complementary metal–oxide semiconductor compatible technique, allows for vertical integration of the optical and electronic devices on the same substrate, thereby improving the device density and enhancing the functionality of the silicon chip. We have demonstrated that the SIMOX 3-D sculpting can be used to realize strained silicon [26]. We consider the stress in silicon waveguides is induced by the volumetric expansion of the SIMOX oxide layer, and the stress was measured via Raman spectroscopy. However, only one single stress value, which represents the stress of the major area inside the silicon waveguide, was measured because the spatial resolution of conventional Raman spectroscopy is restricted by the diffraction limit of light. Furthermore, the strain measurement at the nanometer scale in the SIMOX 3-D sculpted buried silicon waveguide is vital, as mentioned previously. Tip-enhanced Raman spectroscopy (TERS) combines surface-enhanced Raman spectroscopy (SERS) with scanning probe microscopy (SPM) and provides spatial resolution typically down to the nanometer scale [27]. The TERS system has been experimentally realized since 2000 [28] and it is being widely used in the materials science, chemical science and biological science [27]. Although about 20 nm spatial resolution stress is measured on a strained silicon layer grown on SiGe [29], there is no nanoscale strain mapping in an optical silicon waveguide using this technique.

In this paper, we measured, for the first time, the nanoscale strain in the SIMOX 3-D sculpted buried silicon waveguides using TERS. A model, which relates the observed Raman peak shifts to the localized stresses for our TERS experiments, was presented. A 2-D stress map inside the silicon waveguide with spatial resolution of about 20 nm was extracted from the observed Raman peak shifts, and the corresponding strains were calculated based on the Hooke's law. The origins of strain and the strain-induced second order optical susceptibility inside the SIMOX 3-D sculpted buried silicon waveguides are discussed and analyzed.

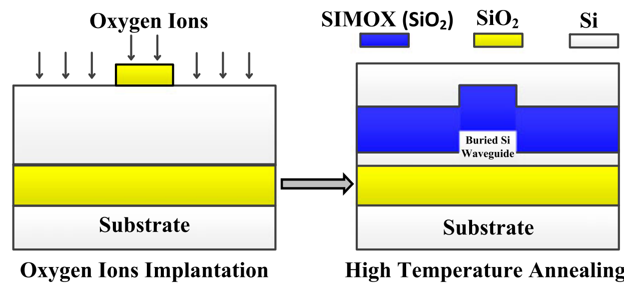

Fig. 1. Schematic of process flow of SIMOX 3-D sculpting to fabricate buried silicon waveguides.

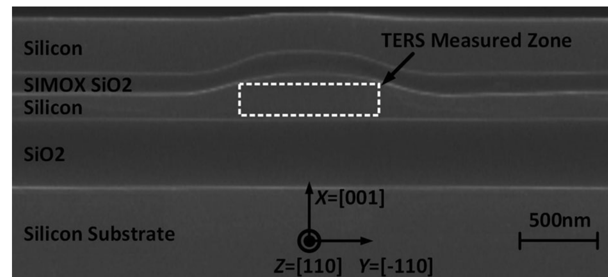

Fig. 2. SEM picture of a buried rib silicon waveguide fabricated using SIMOX 3-D sculpting.

2. Fabrication

The buried silicon waveguides are fabricated using the SIMOX 3-D sculpting, which is a modified form of the SIMOX technology [26]. SIMOX is a well-established commercial technology and conventionally used to realize a buried oxide layer and produce high quality Silicon-On-Insulator (SOI) wafers. Fig. 1 depicts the process flow of SIMOX 3-D sculpting to fabricate buried silicon waveguides. The implantation of oxygen ions is performed on a SOI substrate that has been patterned with thermally grown oxide. Where present, the semi-transparent thermal oxide mask decelerates implanted oxygen ions, which then penetrate into the substrate. Therefore, the oxide mask produces a difference in the penetration depth of the oxygen ions between regions with and without thermal oxide. High temperature annealing annihilates lattice defects and catalyzes the formation of SiO_2. A buried rib silicon waveguide is formed underneath the oxide mask. The thickness and the depth of the buried SIMOX oxide layer are determined by the implantation dose and energy, respectively.

The fabrication of the buried silicon waveguide began with a $<001>$ SOI wafer (made by SOITEC Inc.) with 0.6 μm of silicon on top of a 0.4 μm buried oxide layer. The SOI wafer was thermally oxidized and patterned using reactive ion etching to form an oxide mask of thickness 0.1 μm with a width of 0.8 μm. The patterned wafer was then implanted by oxygen ions having energy of 180 KeV with a dose of $5.0 \times 10^{17}/\text{cm}^2$. Fig. 2 shows the cleaved cross-sectional Scanning Electron Microscope (SEM) photograph of a buried rib silicon waveguide structure that was fabricated using the SIMOX 3-D sculpting technique. It is seen from Fig. 2 that a sub-micrometer buried rib silicon waveguide was formed, which was separated from the top silicon layer by the continuous and Si-island free SIMOX oxide layer.

3. Experimental

Our TERS system consists of a Horiba Jobin Yvon XploRA Plus Raman spectrometer opticaly coupled with a AIST-NT Atomic Force Microscopy (AFM). The TERS system works in the reflection mode with side illumination geometry, which is capable to characterize the opaque samples. The entire TERS system is placed on an optical table to isolate vibration. As shown in Fig. 3(a), the TERS

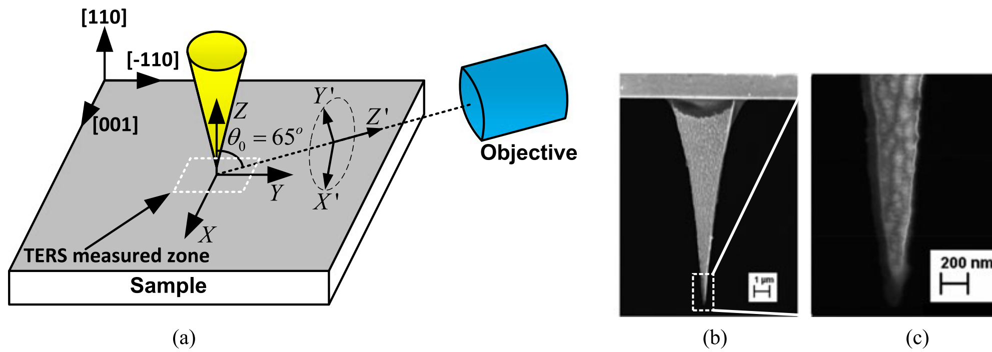

(a) (b) (c)

Fig. 3. (a) Schematic drawing of the TERS experimental configuration, defining the sample reference frame (XYZ) and the laboratory reference frame ($X'Y'Z'$); the axis Z is along the sample surface normal; AFM tip is perpendicular to the sample surface; the axis Z' is along the direction of propagation of light; the axes X, Y and Z are parallel to the [001], [−110], and [110] silicon crystallographic axes, respectively. (b) SEM image of the AFM gold-coated silicon nitride tip. (c) An enlargement of the apical part of the tip, where the curvature diameter of tip apex is about 40 nm.

experiments are performed on the cleaved cross-section [(110) plane] of the silicon waveguide. The sample surface normal and the tip direction are collinear. The dash box is the TERS measured zone as indicated in the Fig. 2. A long working distance objective (Mitutoyo, $\times 100$, 0.7 NA) is tilted at incidence angle θ_0 of 65° with respect to the sample surface normal. Both illumination and collection are realized using this objective. A laser beam at wavelength of 638 nm is focused on the measured zone, producing a diffraction limited spot with size of $0.56 \times 1.31 \times \pi \approx 2.3\ \mu m^2$ (the spot is elliptical because of the oblique geometry). The propagation of the laser beam is along the Z' axis, and the axes Y and Y' are in the scattering plane defined by axes Z and Z'. The polarizations of the incident light and Raman scattered light can be set either along the X' axis (S polarization) or along the Y' axis (P polarization). In order to avoid the sample heating and tip apex deterioration, the laser power is set at 0.2 mW.

The AFM is operated in the non-contact mode with the purpose of avoiding the pressure from the tip on the sample. The AFM tip is perpendicular to the sample surface. For avoiding the Raman spectrum from a Si tip shadow that from the sample, we employ a silicon nitride (SiN) tip in this work. The AFM SiN tip is coated by thermal evaporation with Au. Fig. 3(b) is the SEM image of the AFM gold-coated SiN tip. An enlargement of the apical part of the tip is shown in Fig. 3(c), and it shows the curvature diameter of tip apex is about 40 nm, which is vital to realize nanoscale strain mapping.

4. Modeling

The classic Raman scattering is presented in detail elsewhere [30], and the theory of stress measurement based on the Raman spectrum peak shift for cubic crystals can be found in a number of references [31], [32]. Moreover, numerous phenomenological models were developed to address the particular issues, such as polarization properties, tip amplification and oblique incidence geometry, of the TERS system [33], [34]. Here, we present a model, which relates the observed Raman peak shifts to the stresses for our TERS experiments, based on those reported theories and models [30]–[34]. Our model not only takes into account tip-induced electric-field enhancements and oblique incidence geometry, but includes the tip-induced depolarization of the incident light as well. The model will be utilized to appropriately select both polarizations of the incident light and Raman scattered light and accurately calculate the stresses from the observed Raman peak shifts.

The Raman scattering intensity I is dependent on the electrical field vectors of incident $\boldsymbol{v_i}$ and Raman scattered $\boldsymbol{v_s}$ light, and it is given by

$$\boldsymbol{I} \propto \sum_{k=1}^{3} |\ \boldsymbol{v_s} \cdot \boldsymbol{R_k} \cdot \boldsymbol{v_i}|^2 \tag{1}$$

where $\boldsymbol{R}_k$ is the Raman polarizability tensors.

In a cubic crystal such as silicon, the Raman active optical phonon modes are triply degenerate. However, when strain is applied to silicon, the strain breaks the crystalline symmetry of silicon and the degeneracy is lifted, which results in splitting of Raman modes and modification of Raman polarizability tensors [31]. For silicon, under a diagonal stress tensor in the frame $\{[110], [-110], [001]\}$, the Raman polarizability tensors $\boldsymbol{R}_k^{st}$ are modified as the following forms [35]:

$$R_1^{st} = \frac{1}{\sqrt{2}}\begin{pmatrix} 0 & 0 & 1 \\ 0 & 0 & 1 \\ 1 & 1 & 0 \end{pmatrix}, \; R_2^{st} = \frac{1}{\sqrt{2}}\begin{pmatrix} 0 & 0 & 1 \\ 0 & 0 & -1 \\ 1 & -1 & 0 \end{pmatrix}, \; R_3^{st} = \begin{pmatrix} 0 & 1 & 0 \\ 1 & 0 & 0 \\ 0 & 0 & 0 \end{pmatrix} \tag{2}$$

where the superscript *"st"* denotes that these are Raman polarizability tensors with the presence of strain. Since the TERS experiments performed in this work are on the (110) plane of the silicon waveguide with back scattering, R_1^{st} corresponds to scattering by longitudinal optical phonon modes (LO), while R_2^{st}, R_3^{st} correspond to scattering by transverse optical phonon modes (TO1, TO2), respectively. Moreover, the tip direction, the sample surface normal and the Z axis are collinear. Therefore, the Raman polarizability tensors $\boldsymbol{R}_k^{st}$ can be easily transformed from crystal frame $\{[100], [010]\ [001]\}$ to the frame (XYZ) by

$$\boldsymbol{R}_k^{st} \leftarrow \boldsymbol{T}_{110}^{T} \boldsymbol{R}_k^{st} \boldsymbol{T}_{110} \tag{3}$$

where $\boldsymbol{T}_{110}$ is the transformation matrix (the superscript T stands for the transpose), and it is given by

$$\boldsymbol{T}_{110} = \frac{1}{\sqrt{2}}\begin{bmatrix} 0 & -1 & 1 \\ 0 & 1 & 1 \\ \sqrt{2} & 0 & 0 \end{bmatrix}. \tag{4}$$

When the incident light illuminate the tip, electric-field enhancements and light depolarization occurred simultaneously at the apex of the tip, and these two effects cannot be neglected for evaluating the Raman scattering intensity of the TERS experiments. Electric-field enhancements are induced by interaction of the electromagnetic field with the tip, such as the localized surface plasmon resonance [36] and the lightning-rod effect [37], and it can be modeled by the "tip-amplification tensor" $\boldsymbol{A}$, which is a diagonal representation in the frame (XYZ) [33], namely

$$\boldsymbol{A} = \begin{bmatrix} a & 0 & 0 \\ 0 & a & 0 \\ 0 & 0 & b \end{bmatrix} \tag{5}$$

where a and b ($a < b$) are phenomenological tip-amplification factors, and these factors are determined by the geometry and coating material dielectric constant of the tip. The factor b is larger than a can be explained by the fact that the enhancement is much stronger for the electrical field component along the tip direction than that perpendicular to it [38].

At the same time, as polarized light scattered from non-spherical particles on the tip, there is a non-zero intensity component with polarization orthogonal to the incident one, and the depolarization ratio of the incident light between 5% and 30% has been demonstrated [39]. The depolarization effect is included in our model by introduction of a "depolarization matrix" $\boldsymbol{D}'$, which has the following form in the frame $(X'Y'Z')$:

$$\boldsymbol{D}' = \begin{bmatrix} 1-r & r \\ r & 1-r \end{bmatrix} \tag{6}$$

where r is the depolarization ratio of the intensity of depolarized light to the total intensity of the original one. The depolarization ratio r is dependent on the wavelength and power of the incident light [40], as well as on the geometry and coating material dielectric constant of the tip, and therefore, it is hard to be determined. Here, only the incident light polarization changes of S-to-P

and P-to-S are considered. Since the polarized lights are the transverse wave in the frame ($X'Y'Z'$), and according to the Jones vector form for polarized light, the electrical field vectors can only be described by two components. Therefore the matrix $\boldsymbol{D}'$ has the 2×2 form.

Both tensors $\boldsymbol{R}_k^{st}$ and $\boldsymbol{A}$ are expressed in the sample reference frame (XYZ), which should be transferred to the laboratory reference frame ($X'Y'Z'$). Under the consideration of the oblique backscattering configuration of the TERS system, these tensors can be transferred to the frame ($X'Y'Z'$) by [33]

$$\boldsymbol{A}' = \boldsymbol{F}_{00}^T \boldsymbol{T}_X^T(\theta_0)\boldsymbol{A}\boldsymbol{T}_X(\theta_0)\boldsymbol{F}_{00} \tag{7a}$$

$$\boldsymbol{R}_k^{st\prime} = \boldsymbol{F}_{10}^T \boldsymbol{T}_X^T(\theta_1)\boldsymbol{R}_k^{st}\boldsymbol{T}_X(\theta_1)\boldsymbol{F}_{01} \tag{7b}$$

where $\boldsymbol{T}_X(\theta_m)$, $m = 0,\ 1$ is a transformation matrix which denotes the rotation of a frame about its X axis at an angle θ_m, and it brings the frame (XYZ) into ($X'Y'Z'$), while $\boldsymbol{F}_{ij}$, $i, j = 0, 1$ are the Fresnel matrices, which describe the electric field amplitude changes when the light travels from a medium i to another one j (0 and 1, respectively, denote ambient and silicon in this work).

The transformation matrix $\boldsymbol{T}_x(\theta_m)$ can be expressed as

$$\boldsymbol{T}_X(\theta_m) = \begin{bmatrix} 1 & 0 & 0 \\ 0 & \cos\theta_m & \sin\theta_m \\ 0 & -\sin\theta_m & \cos\theta_m \end{bmatrix},\ m = 0,\ 1 \tag{8}$$

where θ_0 is the incident angle of the light as defined in the Fig. 3(a), while θ_1 is the incident angle in the silicon, which can be defined by the Snell's law

$$n_1 \sin\theta_1 = n_0 \sin\theta_0. \tag{9}$$

In (9), n_1 and n_0 are the refractive index of the silicon and ambient, respectively. The value of n_1 is 3.86 at wavelength of 638 nm, and that of n_0 is 1.

The Fresnel matrices $\boldsymbol{F}_{ij}$ can be given by [33]

$$\boldsymbol{F}_{ij} = \begin{bmatrix} t_{ij}^s & 0 \\ 0 & t_{ij}^p \\ 0 & 0 \end{bmatrix},\ i,\ j = 0,\ 1 \tag{10}$$

where t_{ij}^s and t_{ij}^p are the transmission coefficients for S-polarized (along X' axis) and P-polarized (along Y' axis) incident light respectively, they can be expressed by the Fresnel relations [41]

$$t_{ij}^s = \frac{2n_i\cos\theta_i}{n_i\cos\theta_i + n_j\cos\theta_j},\ t_{ij}^p = \frac{2n_i\cos\theta_i}{n_i\cos\theta_j + n_j\cos\theta_i}. \tag{11}$$

Based on (1), the tip-enhanced Raman scattered field intensity I^{tef} of our TERS experiments is given by

$$I_{hl}^{tef} = \sum_{k=1}^{3} I_{khl}^{tef} \propto \sum_{k=1}^{3} |\, \boldsymbol{e}_s{}'^T \boldsymbol{A}'^T \boldsymbol{R}_k^{st\prime} \boldsymbol{A}'\boldsymbol{D}'\boldsymbol{e}_i{}'|^2 \tag{12}$$

where I_{khl}^{tef} is the Raman scattered intensity for the kth phonon mode under the polarizations configuration hl, $h,\ l \in \{S, P\}$, and h, l correspond to the polarizations of incident and Raman scattered light, respectively; while the $\boldsymbol{e}_i{}'$ and $\boldsymbol{e}_s{}'$ are the electrical field vectors of the incident and scattered light expressed in the laboratory frame ($X'Y'Z'$), respectively. The pre- and post-multiplication of the Raman polarizability tensors $\boldsymbol{R}_k^{st\prime}$ by the tip-amplification tensor $\boldsymbol{A}'$ in (12) accounts for the Raman scattered and incident light amplification, respectively. However, only the depolarization of the incident light is considered in this work, this is realized through post-multiplication of Raman polarizability tensors $\boldsymbol{R}_k^{st\prime}$ by the depolarization matrix $\boldsymbol{D}'$.

The incident $\boldsymbol{e}_i{}'$ and scattered $\boldsymbol{e}_s{}'$ light can be set either as S-polarized or P-polarized light, namely, $\boldsymbol{e}_i{}', \boldsymbol{e}_s{}' \in \{\boldsymbol{v}_S{}', \boldsymbol{v}_P{}'\}$, where $\boldsymbol{v}_S{}'$ and $\boldsymbol{v}_P{}'$ are basic electrical field vectors of S-polarized and P-polarized

light, respectively, and they can only be described by two components in the frame ($X'Y'Z'$) as previously explained, and therefore, they are given by

$$\boldsymbol{v_S}' = \begin{bmatrix} 1 \\ 0 \end{bmatrix}, \quad \boldsymbol{v_P}' = \begin{bmatrix} 0 \\ 1 \end{bmatrix}. \tag{13}$$

For different configurations of polarizations of incident $\boldsymbol{e_i}'$ and scattered $\boldsymbol{e_s}'$ light, based on (12), the observed optical photon modes can be determined. Some of the originally invisible phonon modes become observable as the contributions of the “depolarization effect” or “oblique incidence”. There are visible phonon modes result from the contribution of “depolarization effect” under the polarizations configuration *SS*, *SP* and *PP*, and the corresponding Raman intensities I_{khl}^{tef} are hard to determine because of the unknown depolarization ratio r. However, for the polarizations configuration *PS*, although part of the incident light changes from *P*-polarized to *S*-polarized, there are no observed phonon modes contributed by this depolarized light, so the Raman intensities I_{kps}^{tef} are easily determined. Furthermore, the *P*-polarized incident light, whose electrical field is along the tip direction, can excite larger electric-field enhancements than that for *S*-polarized [38]. Hence, all the TERS experiments will be performed under polarizations configuration *PS* in this work.

For the SIMOX 3-D sculpted silicon waveguide shown in Fig. 2, the stress components σ_{ZZ} along the waveguide direction (Z -direction) and σ_{XX} along X axis can be omitted compared with σ_{YY}. Consequently, the complexity of the stress tensor $\boldsymbol{\sigma}$ is reduced to one component σ_{YY} oriented along the Y-direction [26]. The relation between the stress component σ_{YY} and the Raman peak shifts can be given by [42]

$$\Delta\omega_1 = \frac{1}{2\omega_0}\left\{\left[\left(\frac{p+q}{2}\right)(S_{12}+S_{11}) + qS_{12} - \frac{rS_{44}}{2}\right]\sigma_{YY}\right\} \tag{14a}$$

$$\Delta\omega_2 = \frac{1}{2\omega_0}\left\{\left[\left(\frac{p+q}{2}\right)(S_{12}+S_{11}) + qS_{12} + \frac{rS_{44}}{2}\right]\sigma_{YY}\right\} \tag{14b}$$

$$\Delta\omega_3 = \frac{1}{2\omega_0}\left\{\left[q(S_{12}+S_{11}) + pS_{12}\right]\sigma_{YY}\right\} \tag{14c}$$

where S_{11}, S_{12}, and S_{44}, are the elastic compliance constants, p, q and r are the phonon deformation potentials (PDPs), ω_0 is the Raman frequency of unstrained silicon, and $\Delta\omega_k$, $k = 1, 2, 3$, is Raman peak shift between Raman frequency ω_k of kth phonon mode in the presence of stress and the ω_0. For silicon, $S_{11} = 7.68 \times 10^{-12}$ Pa^{-1}, $S_{12} = -2.14 \times 10^{-12}$ Pa^{-1} and $S_{44} = 12.7 \times 10^{-12}$ Pa^{-1} [43], while $p = -1.85\omega_0^2$, $q = -2.31\omega_0^2$, and $r = -0.71\omega_0^2$ [44].

Since our TERS experiments are performed on the cleaved cross-section of the silicon waveguide, there is no background Raman signal from the silicon substrate. Consequently, only one single Raman peak was observed. The observed frequency shift $\Delta\omega_{obs}$ is a weighted average of the individual Raman peak shifts $\Delta\omega_k$ with their relative intensities I_{khl}^{tef} [45], namely

$$\Delta\omega_{obs} = \frac{\sum_{k=1}^{3}\Delta\omega_k I_{khl}^{tef}}{\sum_{k=1}^{3} I_{khl}^{tef}}. \tag{15}$$

Under the polarizations configuration *PS*, the Raman intensities I_{kps}^{tef} can be calculated based on (12), namely

$$I_{1ps}^{tef} \propto \left[at_{10}^{s}(a\cos^2\theta_0 + b\sin^2\theta_0)(1-r)t_{01}^{p}\sin\theta_1\right]^2 \tag{16a}$$

$$I_{2ps}^{tef} \propto \left[at_{10}^{s}(a\cos^2\theta_0 + b\sin^2\theta_0)(1-r)t_{01}^{p}\cos\theta_1\right]^2 \tag{16b}$$

$$I_{3ps}^{tef} = 0. \tag{16c}$$

Both the LO and TO1 phonon modes can be observed, and $I_{1ps}^{tef}/I_{2ps}^{tef} = (\sin\theta_1/\cos\theta)^2$. It should be noted that LO phonon mode becomes visible under the polarizations configuration *PS* only

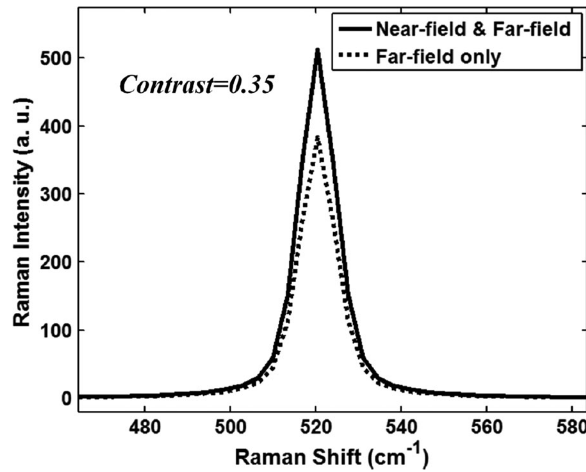

Fig. 4. Raman spectra from the cleaved surface of silicon substrate. (Solid line) Near-field and far-field Raman spectrum measured with the presence of the tip. (Dash line) Far-field Raman spectrum measured when the tip is withdrawn.

due to the oblique incidence backscattering geometry, and this mode is forbidden originally in the conventional confocal backscattering. Then, substituting equation (16) into (15), the linear relation between stress component σ_{YY} and the observed frequency shift $\Delta\omega_{obs}$ can be deduced as follows:

$$\sigma_{YY} = -(\Delta\omega_{obs}/C\omega_0) \times 10^{12}[\text{Pa}] \tag{17}$$

where $C = (1.04 I^{tef}_{1ps} + 5.54 I^{tef}_{2ps})/(I^{tef}_{1ps} + I^{tef}_{2ps}) = 5.29$. Hence, the stress component σ_{YY} inside the SIMOX 3-D sculpted silicon waveguides can be calculated from the measured observed frequency shift $\Delta\omega_{obs}$ using (17).

5. Results

In order to evaluate the feasibility of the TERS system for nanoscale strain mapping in the SIMOX 3-D sculpted silicon waveguides, the *contrast*, which is defined as the ratio of near-field spectrum intensity I_{near} to the far-field spectrum intensity I_{far}, is measured. The *contrast* is expressed as [46]

$$Contrast = \frac{I_{near}}{I_{far}} = \left(\frac{I_{total}}{I_{far}} - 1\right) \tag{18}$$

where I_{total} is the measured intensity with the presence of the tip, and it is the sum of the near-field and far-field spectrum intensity, while I_{far} is the far-field spectrum intensity measured when the tip is withdrawn. Fig. 4 are the Raman spectra from the cleaved surface of silicon substrate using our TERS system under the polarizations configuration *PS*. With this configuration, a *contrast* of 0.35 is attained for our TERS system, which is sufficient to probe the nanoscale strain in the SIMOX 3-D sculpted silicon waveguides. Since the Raman spectra shown in Fig. 4 are obtained far from the silicon waveguide, its peak of 520.6 cm^{-1} can be viewed as the ω_0 for the unstrained silicon.

The TERS experiments are performed on the TERS measured zone as shown in Fig. 2. The TERS spectra were obtained by moving the sample stage with 20 nm steps in the X and Y direction. A total of 10×45 points are recorded, and the acquisition time of each point set at 7 s for collecting enough Raman intensity, resulting in the total recording time of about 53 minutes. The spectra are fitted with a Lorentzian function to extract the central position of the silicon Raman peak. The observed Raman peak shifts $\Delta\omega_{obs}$ at each point were shown in Fig. 5, and the corresponding stresses σ_{YY} are calculated using the equation (17). We consider that the compression from the volumetric expansion of the SIMOX oxide layer applied on the silicon waveguide in the Y -direction, especially

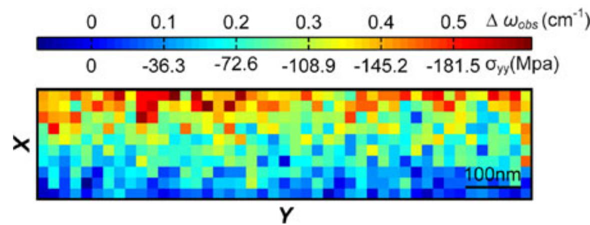

Fig. 5. Observed Raman peak shifts $\Delta\omega_{obs}$ mapped by TERS experiment and the corresponding stress component σ_{YY} inside the SIMOX 3-D sculpted silicon waveguide.

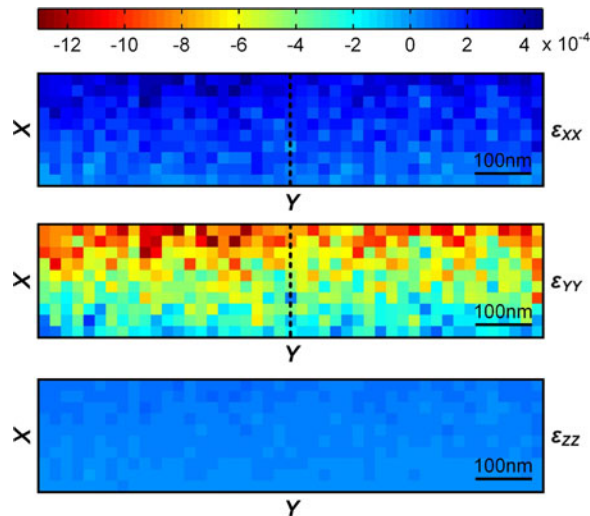

Fig. 6. Maps of strain tensor components ε_{XX}, ε_{YY}, and ε_{ZZ} inside the SIMOX 3-D sculpted silicon waveguide calculated by means of Hooke's law.

on the upper area of the waveguide, resulting in the compressive stresses in the waveguide, and the stresses of the upper area of the waveguide are larger that of the lower area, as shown in Fig. 5. The stresses of the upper area are mainly in the range of -140–-200 Mpa, while the stresses in the lower area range from -30 to -70 Mpa. It should be noted that the stresses are slightly different from the stresses reported in our paper [26] because the silicon waveguide is different from the one used in that article. Although these two silicon waveguides are fabricated under the same conditions, their dimension are different, which may the reason for the slight difference of the stress.

The strains in the silicon waveguide are calculated by means of Hooke's law, as shown in the Fig. 6. The strain component ε_{YY} is dominated because we consider the compression from the volumetric expansion of SIMOX oxide layer mainly applied in the Y-direction, and the compression in the X -direction can be easily relaxed, resulting in the strain component ε_{XX} is smaller than ε_{YY}. While the strain component ε_{ZZ} along the waveguide direction is negligible compared with the other two strain components, since only a plane stress is investigated in the silicon waveguide. It should be noted that strain component ε_{YY} is compressive while strain components ε_{XX} and ε_{ZZ} are tensile. This can be explained by the theory of elasticity, a material compressed in one direction normally tends to expand in the other perpendicular directions and *vice versa*. We can observe that the strain in the Y-direction of the waveguide is inhomogeneous, and it can break the symmetry of silicon's crystal lattice.

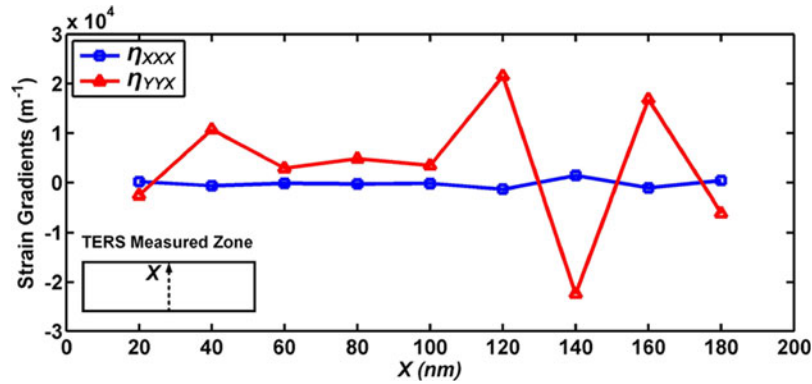

Fig. 7. Strain gradients components η_{XXX} and η_{YYX} over the vertical dashed black line, as shown in Fig. 6.

6. Discussions

The stress in the SIMOX 3-D sculpted silicon waveguide can be understood as the competition between stress inducing oxide formation and stress relieving high-temperature annealing, which have been analyzed in our paper [26]. Simply, the reaction of silicon atoms and implanted oxygen ions lead to formation of SiO_2, and oxidation is accompanied by large volumetric expansion, which induces stress in the silicon waveguide. However, the stress will be relieved with the time during high temperature annealing since SiO_2 presents viscoelastic behavior at high temperature. Both stress formation and stress relaxation are temperature and time dependent, and therefore, the stress in the silicon waveguide can be controlled by adjusting the parameters of SIMOX process. Noted that, although we ascribe the strain inside the SIMOX 3-D sculpted silicon waveguides to the volumetric expansion of the SIOMX oxide layer, the defects and dislocation caused by the oxygen ions implantation may the origins for the presence of strain as well.

When inhomogeneous strain is applied to silicon, the inhomogeneous strain will change the polarity of a Si-Si bond and create $\chi^{(2)}$ in silicon [15]. In addition, it is widely accepted that there is a relation between $\chi^{(2)}$ and strain gradients [13]–[15], [18], [19], [21], [22]. The strain gradients components η_{XXX} and η_{YYX} in the center of the SIMOX 3-D sculpted silicon waveguide are determined, as shown in Fig. 7. Therefore, the magnitude of $\chi^{(2)}$ inside the silicon waveguide can be estimated based on the theoretical model presented in [15], namely

$$\chi^{(2)}_{YYX} \sim 8.0 \times 10^{-17}(\mathrm{m}^2/\mathrm{V})\eta_{XXX} + 4.6 \times 10^{-17}(\mathrm{m}^2/\mathrm{V})\eta_{YYX}. \tag{19}$$

Considering that the electromagnetic modes are mainly focused in the center of the silicon waveguide, by utilizing the strain gradients from the center of the waveguide, namely, $\eta_{YYX} \approx 2.2 \times 10^4 m^{-1}$ and $\eta_{XXX} \approx -1.4 \times 10^3 m^{-1}$, we can get

$$\chi^{(2)}_{YYX} \sim 0.9\mathrm{pm/V}. \tag{20}$$

The estimated $\chi^{(2)}_{YYX}$ value has the same order of magnitude as the strain-induced $\chi^{(2)}$ reported in [17], but it is too small for practical application. However, the strain distribution in the SIMOX 3-D sculpted silicon waveguide can be engineered by adjusting the parameters of SIMOX process, such as annealing time and annealing temperature [26]. Therefore, it is possible to increase the $\chi^{(2)}$ value by optimizing the strain gradients. Furthermore, the total second order optical susceptibility $\chi^{(2)}$ in the silicon waveguide should be a weighted average of the spatially distributed $\chi^{(2)}$ with the electromagnetic mode [21]. Therefore, through designing of waveguide geometry to enhance the overlap between the strain gradients and the electric field of the optical mode, it's possible to make the SIMOX 3-D sculpted silicon waveguide to be a practical material for electro-optical modulation and optical signal processing.

7. Conclusion

In this paper, the distribution of stress on the facet of a SIMOX 3-D sculpted silicon waveguide has been measured using TERS for the first time. The TERS system is realized by optically coupling of a Raman spectrometer and an atomic force microscopy (AFM) operated in the non-contact mode with side illumination. A model, which takes into account tip-induced electric-field enhancements, tip-induced depolarization of incident light and oblique incidence geometry for our TERS experiment, was presented. The model was utilized to appropriately select polarizations of incident light and Raman scattered light, and accurately calculate the stresses from the observed Raman peak shifts. A two-dimensional stress map inside the silicon waveguide with spatial resolution of about 20 nm was obtained. We observed the stresses are compressive and stresses in the area close to the interface of silicon waveguide/SIMOX oxide layer are larger than that of other areas of the silicon waveguide. The corresponding strains were calculated based on the Hooke's law, and the strains show inhomogeneity, which may break the symmetry of silicon's crystal lattice. The origins of strain and the strain-induced second order optical susceptibility inside the SIMOX 3-D sculpted buried silicon waveguides are discussed and analyzed.

The mapping of two-dimensional inhomogeneous nanoscale strain and the analysis of the second order optical susceptibility inside SIMOX 3-D sculpted silicon waveguides suggest that this kind of silicon waveguides might be a potential metamaterial for electro-optical modulation and optical signal processing. Moreover, the presented TERS model could be a valuable tool for probing strain in strained silicon devices. We hope that this work will stimulate efforts on developing practical SIMOX 3-D sculpted strained-silicon-based active components for silicon photonics and optical networks.

Acknowldgment

The authors would like to thank Dr. M. Chaigneau from HORIBA Scientific, Dr. D. Voylov from the University of Tennessee for help and fruitful discussions on the TERS experiments, and Dr. K. Kishima for providing the SIMOX 3-D sculpted silicon waveguides.

References

[1] Y. Ji, X. Wang, S. Zhang, R. Gu, T. Guo, and Z. Ge, "Dual-layer efficiency enhancement for future passive optical network," *Sci. China Inf. Sci.*, vol. 59, no. 2, pp. 1–13, 2016.
[2] H. Wang, J. Zhao, H. Li, and Y. Ji, "Opaque virtual network mapping algorithms based on available spectrum adjacency for elastic optical networks," *Sci. China Inf. Sci.*, vol. 59, pp. 1–11, 2016.
[3] C. V. Saradhi and S. Subramaniam, "Physical layer impairment aware routing (PLIAR) in WDM optical networks: Issues and challenges," *IEEE Commun. Surveys Tuts.*, vol. 11, pp. 109–130, 2009.
[4] D. Zhao, K. Long, Y. Zheng, J. Sun, and W. Gong, "Channel power control in optical amplifiers to mitigate physical impairment in optical network," *Sci. China Inf. Sci.*, vol. 58, no. 10, pp. 1–8, 2015.
[5] B. Jalali and S. Fathpour, "Silicon photonics," *J. Lightw. Tech.*, vol. 24, no. 12, pp. 4600–4615, 2006.
[6] O. Boyraz and B. Jalali, "Demonstration of a silicon Raman laser," *Opt. Exp.*, vol. 12, pp. 5269–5273, 2004.
[7] G. T. Reed, G. Mashanovich, F. Y. Gardes, and D. J. Thomson, "Silicon optical modulators," *Nature Photon.*, vol. 4, pp. 518–526, 2010.
[8] T. K. Liang and H. K. Tsang, "Efficient Raman amplification in silicon-on-insulator waveguides," *Appl. Phys. Lett.*, vol. 85, pp. 3343–3345, 2004.
[9] R. Salem, M. A. Foster, A. C. Turner, D. F. Geraghty, M. Lipson, and A. L. Gaeta, "Signal regeneration using low-power four-wave mixing on silicon chip," *Nature Photon.*, vol. 2, pp. 35–38, 2008.
[10] Ö. Boyraz, P. Koonath, V. Raghunathan, and B. Jalali, "All optical switching and continuum generation in silicon waveguides," *Opt. Exp.*, vol. 12, pp. 4094–4102, 2004.
[11] R. S. Jacobsen *et al.*, "Strained silicon as a new electro-optic material," *Nature*, vol. 441, pp. 199–202, 2006.
[12] B. Chmielak *et al.*, "Pockels effect based fully integrated, strained silicon electro-optic modulator," *Opt. Exp.*, vol. 19, pp. 17212–17219, 2011.
[13] B. Chmielak *et al.*, "Investigation of local strain distribution and linear electro-optic effect in strained silicon waveguides," *Opt. Exp.*, vol. 21, pp. 25324–25332, 2013.
[14] P. Damas *et al.*, "Wavelength dependence of Pockels effect in strained silicon waveguides," *Opt. Exp.*, vol. 22, pp. 22095–22100, 2014.
[15] P. Damas, D. Marris-Morini, E. Cassan, and L. Vivien, "Bond orbital description of the strain-induced second-order optical susceptibility in silicon," *Phys. Rev. B*, vol. 93, p. 165208, 2016.

[16] S. Sharif Azadeh, F. Merget, M. P. Nezhad, and J. Witzens, “On the measurement of the Pockels effect in strained silicon,” *Opt. Lett.*, vol. 40, pp. 1877–1880, 2015.
[17] M. Borghi *et al.*, “High-frequency electro-optic measurement of strained silicon racetrack resonators,” *Opt. Lett.*, vol. 40, pp. 5287–5290, 2015.
[18] M. Cazzanelli *et al.*, “Second-harmonic generation in silicon waveguides strained by silicon nitride,” *Nature Mater.*, vol. 11, pp. 148–154, 2012.
[19] C. Schriever *et al.*, “Second-Order Optical Nonlinearity in Silicon Waveguides: Inhomogeneous Stress and Interfaces,” *Adv. Opt. Mater.*, vol. 3, pp. 129–136, 2014.
[20] J. B. Khurgin, T. H. Stievater, M. W. Pruessner, and W. S. Rabinovich, “On the origin of the second-order nonlinearity in strained Si-SiN structures,” *J. Opt. Soc. Amer. B*, vol. 32, pp. 2494–2499, 2015.
[21] C. L. Manganelli, P. Pintus, and C. Bonati, “Modeling of strain-induced Pockels effect in Silicon,” *Opt. Exp.*, vol. 23, pp. 28649–28666, 2015.
[22] M. W. Puckett, J. S. T. Smalley, M. Abashin, A. Grieco, and Y. Fainman, “Tensor of the second-order nonlinear susceptibility in asymmetrically strained silicon waveguides: Analysis and experimental validation,” *Opt. Lett.*, vol. 39, no. 6, pp. 1693–1696, 2014.
[23] N. K. Hon, K. K. Tsia, D. R. Solli, B. Jalali, and J. B. Khurgin, “Stress-induced chi(2) in silicon—Comparison between theoretical and experimental values,” in *Proc. 6th IEEE Int. Conf. Group IV Photon.*, 2009, pp. 232–234.
[24] M. L. Lee, E. A. Fitzgerald, M. T. Bulsara, M. T. Currie, and A. Lochtefeld, “Strained Si, SiGe, and Ge channels for high-mobility metal-oxide-semiconductor field-effect transistors,” *J. Appl. Phys.*, vol. 97, 2005, Art. no. 011101.
[25] K. K. Tsia, S. Fathpour, and B. Jalali, “Electrical tuning of birefringence in silicon waveguides,” *Appl. Phys. Lett.*,vol. 92, no. 6, 2008, Art. no. 061109.
[26] H. Wen, D. Borlaug, H. Wang, Y. Ji, and B. Jalali, “Engineering strain in silicon using SIMOX 3-D sculpting,” *IEEE Photon. J.*, vol. 8, pp. 1–9, 2016.
[27] N. Kumar, S. Mignuzzi, W. Su, and D. Roy, “Tip-enhanced Raman spectroscopy: Principles and applications,” *EPJ Tech. Instrum.*, vol. 2, pp. 1–23, 2015.
[28] R. M. Stöckle, Y. D. Suh, V. Deckert, and R. Zenobi, “Nanoscale chemical analysis by tip-enhanced Raman spectroscopy,” *Chem. Phys. Lett.*, vol. 318, pp. 131–136, 2000.
[29] Y. Saito, M. Motohashi, N. Hayazawa, and S. Kawata, “Stress imagining of semiconductor surface by tip-enhanced Raman spectroscopy,” *J. Microscopy*, vol. 229, pp. 217–222, 2008.
[30] R. Loudon, “The Raman effect in crystals,” *Adv. Phys.*, vol. 13, pp. 423–482, 1964.
[31] E. Anastassakis, A. Pinczuk, E. Burstein, F. H. Pollak, and M. Cardona, “Effect of static uniaxial stress on the Raman spectrum of silicon,” *Solid State Commun.*, vol. 8, pp. 133–138, 1970.
[32] I. D. Wolf, “Micro-Raman spectroscopy to study local mechanical stress in silicon integrated circuits,” *Semicond. Sci. Technol.*, vol. 11, p. 139, 1996.
[33] R. Ossikovski, Q. Nguyen, and G. Picardi, “Simple model for the polarization effects in tip-enhanced Raman spectroscopy,” *Phys. Rev. B*, vol. 75, 2007, Art. no. 045412.
[34] R. Ossikovski, Q. Nguyen, G. Picardi, and J. Schreiber, “Determining the stress tensor in strained semiconductor structures by using polarized micro-Raman spectroscopy in oblique backscattering configuration,” *J. Appl. Phys.*, vol. 103, 2008, Art. no. 093525.
[35] I. De Wolf, H. E. Maes, and S. K. Jones, “Stress measurements in silicon devices through Raman spectroscopy: Bridging the gap between theory and experiment,” *J. Appl. Phys.*, vol. 79, pp. 7148–7156, 1996.
[36] B. Pettinger, B. Ren, G. Picardi, R. Schuster, and G. Ertl, “Nanoscale probing of adsorbed species by tip-enhanced raman spectroscopy,” *Phys. Rev. Lett.*, vol. 92, 2004, Art. no. 096101.
[37] M. Asghari-Khiavi *et al.*, “Exploring the origin of tip-enhanced Raman scattering; preparation of efficient TERS probes with high yield,” *J. Raman Spectroscopy*, vol. 43, pp. 173–180, 2012.
[38] L. Aigouy, A. Lahrech, S. Grésillon, H. Cory, A. C. Boccara, and J. C. Rivoal, “Polarization effects in apertureless scanning near-field optical microscopy an experimental study,” *Opt. Lett.*, vol. 24, pp. 187–189, 1999.
[39] P. G. Gucciardi, M. Lopes, R. Déturche, C. Julien, D. Barchiesi, and M. L. d. l. Chapelle, “Light depolarization induced by metallic tips in apertureless near-field optical microscopy and tip-enhanced Raman spectroscopy,” *Nanotechnol.*, vol. 19, 2008, Art. no. 215702.
[40] A. Merlen, J. C. Valmalette, P. G. Gucciardi, M. L. de la Chapelle, A. Frigout, and R. Ossikovski, “Depolarization effects in tip-enhanced Raman spectroscopy,” *J. Raman Spectroscopy*, vol. 40, pp. 1361–1370, 2009.
[41] M. Born and E. Wolf, *Principles of Optics*. Cambridge, U.K.: Cambridge Univ. Press, 2005, Chap. 1, p. 42.
[42] F. Bianco *et al.*, “Two-dimensional micro-Raman mapping of stress and strain distributions in strained silicon waveguides,” *Semicond. Sci. Technol.*, vol. 27, p. 085009, 2012.
[43] J. J. Wortman and R. A. Evans, “Young’s modulus, shear modulus, and poisson’s ratio in silicon and germanium,” *J. Appl. Phys.*, vol. 36, pp. 153–156, 1965.
[44] E. Anastassakis, A. Cantarero, and M. Cardona, “Piezo-Raman measurements and anharmonic parameters in silicon and diamond,” *Phys. Rev. B*, vol. 41, pp. 7529–7535, 1990.
[45] T. Miyatake, A. A. Porporati, and G. Pezzotti, “Spatially and tensor-resolved Raman analysis for the determination of phonon deformation potentials on the microscopic scale in Si single-crystal,” *J. Appl. Phys.*, vol. 105, 2009, Art. no. 113514.
[46] A. Tarun, N. Hayazawa, and S. Kawata, “Tip-enhanced Raman spectroscopy for nanoscale strain characterization,” *Anal. Bioanal. Chem.*, vol. 394, pp. 1775–1785, 2009.